ACS APPLIED MATERIALS & INTERFACES

www.acsami.org

Research Article

Complete Strain Mapping of Nanosheets of Tantalum Disulfide

Yue Cao,* Tadesse Assefa, Soham Banerjee, Andrew Wieteska, Dennis Zi-Ren Wang, Abhay Pasupathy, Xiao Tong, Yu Liu, Wenjian Lu, Yu-Ping Sun, Yan He, Xiaojing Huang, Hanfei Yan, Yong S. Chu, Simon J. L. Billinge, and Ian K. Robinson*

Cite This: *ACS Appl. Mater. Interfaces* 2020, 12, 43173–43179

Read Online

ACCESS | Metrics & More | Article Recommendations | Supporting Information

ABSTRACT: Quasi-two-dimensional (quasi-2D) materials hold promise for future electronics because of their unique band structures that result in electronic and mechanical properties sensitive to crystal strains in all three dimensions. Quantifying crystal strain is a prerequisite to correlating it with the performance of the device and calls for high resolution but spatially resolved rapid characterization methods. Here, we show that using fly-scan nano X-ray diffraction, we can accomplish a tensile strain sensitivity below 0.001% with a spatial resolution of better than 80 nm over a spatial extent of 100 μm on quasi-2D flakes of 1T-TaS_2. Coherent diffraction patterns were collected from a ∼100 nm thick sheet of 1T-TaS_2 by scanning a 12 keV focused X-ray beam across and rotating the sample. We demonstrate that the strain distribution around micron- and submicron-sized "bubbles" that are present in the sample may be reconstructed from these images. The experiments use state-of-the-art synchrotron instrumentation and will allow rapid and nonintrusive strain mapping of thin-film samples and electronic devices based on quasi-2D materials.

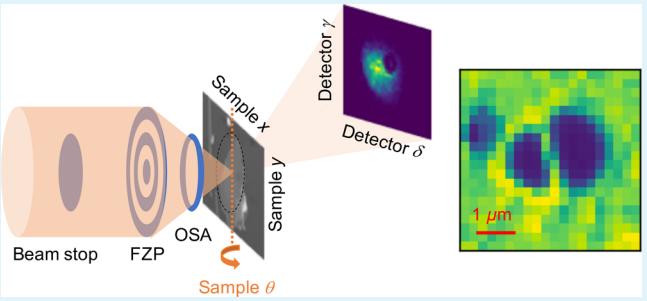

KEYWORDS: *quasi-2D materials, nano X-ray diffraction, strain tensor, strain mapping, Young's modulus*

INTRODUCTION

The lattice degree of freedom profoundly affects the electronic properties of quasi-two-dimensional (quasi-2D) materials ranging from graphene to transition metal dichalcogenides (TMDCs). The stacking of layers,[1−4] in-plane strain,[5] and strong electron−phonon coupling[6−8] among other factors determine the band structures and electron density of states as well as emergent charge orders[9−11] and superconductivity[12] in these materials. Moreover, quasi-2D materials are noted for their highly anisotropic mechanical properties, including superior strength[13,14] in the 2D plane, and have been used as electromechanical resonators.[15] Both observations put the measurement of strains in a critical position—such measurements will provide the basis for quantifying and simulating all other material properties, both electronic and mechanical.

To date, nanoscale strains in quasi-2D materials have been measured almost exclusively using nanoindentation,[13,14,16] where an atomic force microscopy (AFM) tip exerts a force normal to the 2D plane in contact mode before it punctures through. This is an intrusive method and requires free-standing quasi-2D materials. Moreover, deriving the Young's modulus and strain from these measurements often involves rigorous modeling and certain presumptions such as the morphology of the free-standing membrane.

To achieve truly model-independent, nondestructive, and spatial-resolved measurements of the strain tensor, one needs to turn to diffraction-based methods. The key perspective is to consider the entire quasi-2D crystal as consisting of a nanoscale array of 2D "tiles" each with their own lattice parameter and orientations. Strain in the continuous material can then be viewed as originating from seamlessly connecting neighboring tiles. The differences in the lattice parameters and relative orientations of each tile are normally referred to as "mosaic" in the crystallography terminology and give rise to the movements of the Bragg peak, as well as the geometrical differences in satisfying the Bragg condition. We could capture the variation of the Bragg peak positions by scanning a small X-ray beam across the sample. As for the Bragg condition, it is possible to vary the sample orientation at each position in real space and identify the scattering angles that maximize the Bragg peak intensity. To date, such a capability has been demonstrated at the ID-01 (microdiffraction imaging) beamline of the European Synchrotron Radiation Facility (ESRF) and elsewhere but has been limited to fabricated toy models made of Si and related film structures.[17−19]

Received: April 9, 2020
Accepted: August 24, 2020
Published: August 24, 2020

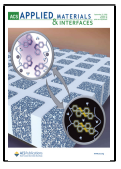

https://dx.doi.org/10.1021/acsami.0c06517
ACS Appl. Mater. Interfaces 2020, 12, 43173−43179

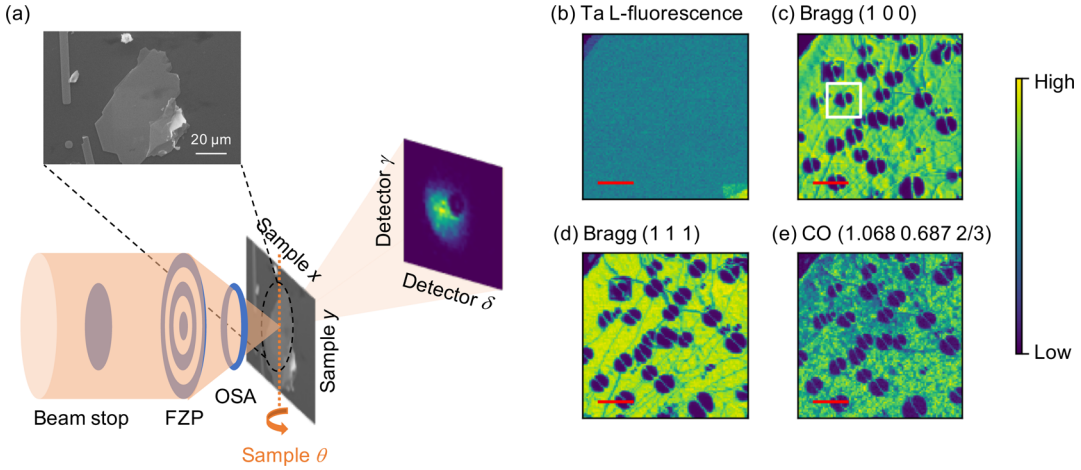

Figure 1. (a) Experimental setup. Monochromatic 12 keV X-rays with 80% coherence are focused using a FZP and pass through an optical sorting aperture onto the sample. The diffracted X-rays are collected using a pixel array detector behind the sample. The geometrical axes and coordinates used throughout the article are as labeled. (b–e) Maps of (b) Ta L-edge fluorescence, (c–e) total scattering intensity at Bragg (1, 0, 0), (1, 1, 1) and charge order (1.068, 0.687, 2/3) peaks. The red solid line corresponds to 5 μm. Each of (c–e) panels is collected at one respective θ angle, which is defined crystallographically as where most of the 1T-TaS_2 sheet satisfies the respective Bragg condition.

In this article, we demonstrate strain mapping in quasi-2D 1T-TaS_2 flakes using X-ray nanodiffraction (nanoXRD). 1T-TaS_2 has been extensively studied as a model TMDC with multiple charge-ordered phases proximate to its onset of superconductivity. It is a Mott insulator with a $\sqrt{13} \times \sqrt{13} \times 3$ commensurate charge order below 200 K and undergoes a first-order metal–insulator transition into the nearly commensurate charge-ordered phase. Another phase transition occurs at 350 K into the incommensurate charge-ordered phase with the ordering vector (0.283, 0, and 1/3).[12,20] Recent theoretical and experimental studies have suggested[6,7,11] that the inter and intralayer strains and electron–phonon coupling impact the macroscopic properties of this material, including the formation and stability of the charge orders. Here, we focus on the strain mapping at room temperature in the nearly commensurate charge-ordered phase.

EXPERIMENTAL METHODS

Figure 1a depicts the nanoXRD geometry. 1T-TaS_2 flakes were exfoliated mechanically and transferred to a 10 μm-thick Si substrate. All the data presented in this article come from a ~100 nm thick sheet of 1T-TaS_2. A scanning electron microscopy image of the nanosheet is also displayed in Figure 1a. Details on material synthesis and sample preparation are described in the Supporting Information. The nanoXRD measurements were performed at room temperature and in a ~300 Torr helium gas (He) environment at the 3-ID (Hard X-ray Nanoprobe) beamline of the National Synchrotron Light Source II, Brookhaven National Laboratory.[21,22] Monochromatic X-rays with a photon energy of 12 keV and 80% coherence were focused by a Fresnel zone plate (FZP) onto the sample with a full width at half-maximum (fwhm) of 80–100 nm. Tight X-ray focus with fwhm of ~50 nm was more often used at the beamline. A larger-than-usual focus was chosen in our case to avoid radiation damage to the charge order in 1T-TaS_2 (but not any of the structural Bragg peaks). The X-ray fluorescence from the sample was collected using a Vortex detector placed 90° relative to the incident X-rays. The diffracted X-rays, transmitted through the sample and the thin substrate, were collected using a pixel-array detector (Merlin with Medipix3 chip) in a forward scattering geometry. As the penetration depth of the X-ray is calculated to be ~3.5 μm, the diffracted X-ray photons come from the entire thickness of the sample rather than the top one or few atomic layers as in the surface-sensitive characterization methods. A detailed description of the beamline and the sample prealignment procedure is described in the Supporting Information and in ref 19. A typical diffraction pattern is shown in Figure 1a. The diffraction intensity is distributed around a central dark region as is typical in coherent nanodiffraction experiments.[23–26] This central dark region originates from the use of a direct beam stop upstream of the FZP. The definition of diffraction angles in this article follows the convention used in a six-circle X-ray diffraction geometry,[27] as illustrated in Figure 1a. Two angles—sample tilt and azimuthal rotation (not drawn)—are limited by the instrumentation and kept constant throughout the experiment. The Bragg condition is uniquely defined by the sample rotation θ (with the rotation axis in the sample plane and normal to the experimental floor), the detector angles δ and γ.

RESULTS AND DISCUSSION

In Figure 1b–e, we show the maps of the Ta L-edge fluorescence intensity and the integrated peak intensities on the area detector at a number of Bragg reflections. Maps shown here and elsewhere in this article are collected by rastering in the sample plane with a dwell time of 0.1 s using the "fly-scan" mode.[28] The continuous scan mode is chosen to minimize the scanning overhead associated with stop-start of the piezo stages.[18] Most prominent in Figure 1c–e are the circular regions with a meridional bar, resembling "coffee-beans". The beans appear dark in their interior indicating a suppressed Bragg peak intensity. Integrated peak intensity maps at more Bragg and charge ordering peaks with different combinations of (H K L) have been obtained all showing the "coffee beans" at the same location, apart from the different pointing of the "meridional bar", which we will explain later in this article. At any given spatial location on the nanosheet, the Bragg peaks could be refined using the same set of crystal orientation matrix defined locally on that location and all with the lattice constant $a = b = 3.35$ Å, $c = 5.86$ Å, $\alpha = \beta = 90°$, and $\gamma = 120°$. Because the Ta fluorescence does not show any changes in these regions, these observations collectively suggest that the missing intensities in the "coffee-bean" regions are due to the sample locally not fully satisfying the Bragg condition as the rest of the bright regions.

To understand the nature of these "coffee bean" profiles, we collected nanoXRD maps at a series of θ angles. The summed intensities from the (1, 0, 0) Bragg peak are displayed in Figure

https://dx.doi.org/10.1021/acsami.0c06517
ACS Appl. Mater. Interfaces 2020, 12, 43173–43179

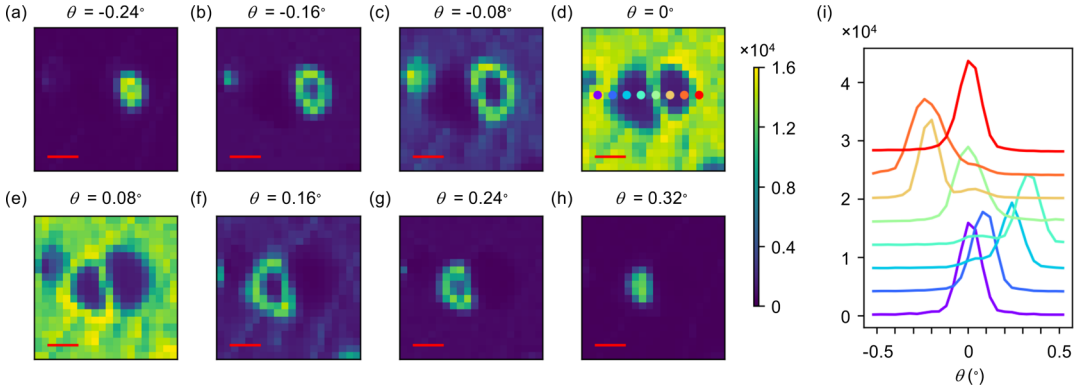

Figure 2. (a–h) NanoXRD diffraction intensity maps of the Bragg peak (1, 0, 0) at different θ angles measured from a 5 μm × 5 μm area as marked using a white solid box in Figure 1. The red solid line corresponds to 1 μm. The θ values are defined relative to the Bragg angle of the "unperturbed" or flat region (the bright part in panel (d) outside the coffee bean). (i) Summed diffraction intensity vs θ angles at selected locations across the "coffee bean". The curves are offset vertically for clarity. The colors of curves correspond the locations marked in panel (d).

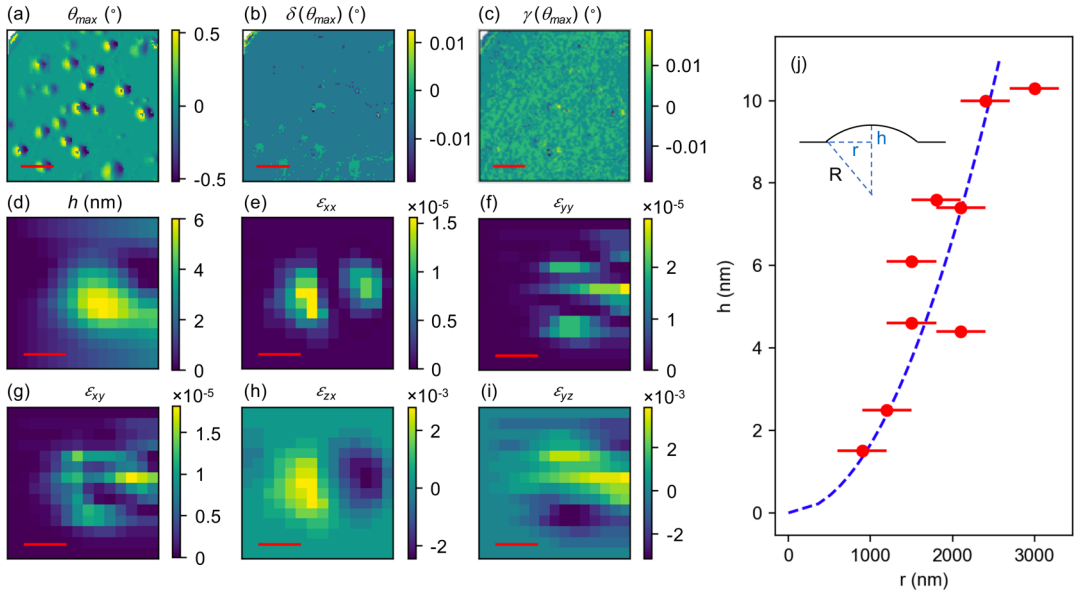

Figure 3. (a) θ angle with maximum Bragg (1, 0, 0) diffraction intensity at different locations on the 1T-TaS_2 nanosheet, labeled as θ_{max}. (b,c) Center of mass of the diffraction pattern at θ_{max} along detector angles δ and γ, labeled as $\delta(\theta_{max})$ and $\gamma(\theta_{max})$. All the units in (a–c) are in degrees, and the red scale bars correspond to 5 μm. (d) Height of the sample normal to the quasi-2D plane and normal to the underlying silicon wafer in the unit of nm. (e–i) Maps of all the nonzero and unequivalent components of the elastic tensor calculated from the sample height in (d). Three of these terms, ε_{xx}, ε_{yy}, and ε_{xy} (e–g), are second order terms, while ε_{zx} and ε_{yz} (h–i) are linear terms. All the scale bars in (e–i) are 1 μm. (j) Radii r and the height h of a few nanobubbles. The inset shows a 1D schematic of a nanobubble. The error bar in the main panel is chosen to be the step size used in the scanning experiments. The dashed blue line is a fit for obtaining the surface curvature R of the nanobubble.

2a–h through a rocking curve. As the θ angle increases monotonically, the bright parts develop from a single point (Figure 2a) to a deformed circle inside the left side of the coffee bean (Figure 2b,c). In Figure 2d,e, the majority of the sample (which we refer to as the unperturbed region, as compared with those close to and within the "coffee bean") meet the Bragg condition and exhibit the maximum scattering intensity. From Figure 2f–h, the right circumference of the coffee bean lights up, shrinks to a deformed circle, and eventually develops a point inside the right side of the coffee bean. The θ values marked on top of Figure 2a–h and throughout the rest of the article are θ angles relative to the Bragg angle of the unperturbed region. We further track the collected nanoXRD intensity versus θ angle at a series of locations across one of the "coffee beans" (Figure 2i). Each of these curves takes on a Lorentzian line shape. The fwhm of each Lorentzian profile is around ~0.2°, corresponding to a correlation length of ~30 nm. The centroids of the peaks are seen to undergo a resonance-like oscillation, distinct at each spatial location.

In Figure 2 for any given location in the projected 2D sample plane, the Bragg diffraction intensity reaches a maximum when the location satisfies a specific Bragg condition. We consider each location as a small tile with independent lattice parameters and orientations. To quantify these parameters at each location, we record the scattering geometry, including θ as well as the position of the diffraction peak on the detector, conventionally denoted by the angles δ (horizontal) and γ (vertical) (Figure 1a). In Figure 3a, we plot the θ angle with the maximum Bragg intensity (denoted as θ_{max}). At θ_{max}, we further determine the center of mass of the diffraction pattern (as shown in Figure 1a) and show the

https://dx.doi.org/10.1021/acsami.0c06517
ACS Appl. Mater. Interfaces 2020, 12, 43173–43179

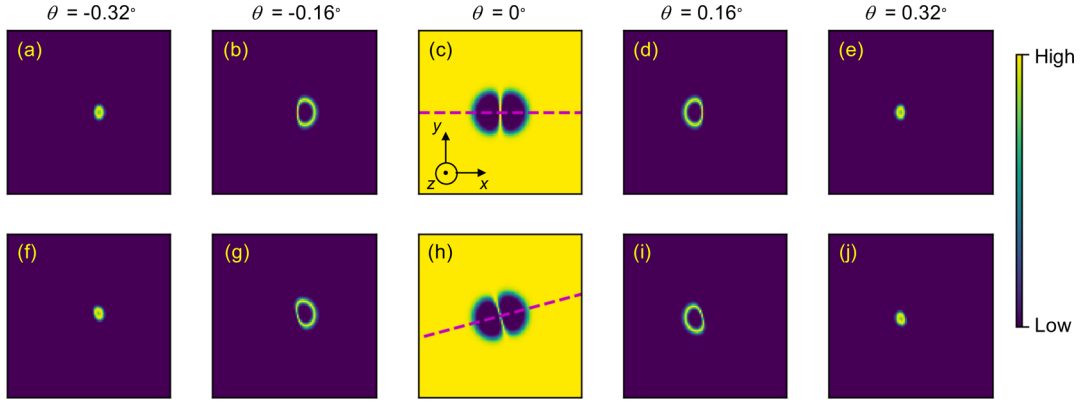

Figure 4. Simulated diffraction intensity maps from a 5 nm high nanobubble at a series of θ angles. The scattering planes in (a–e) are in the z–O–x and in (f–j) are 15° rotated counterclockwise around the z-axis. Projections of the scattering planes in the quasi-2D plane are marked using dashed purple lines in (c,h), respectively.

horizontal and vertical component of the center of mass in Figure 3b,c [denoted as $\delta(\theta_{max})$ and $\gamma(\theta_{max})$]. Notably, the maps of $\delta(\theta_{max})$ and $\gamma(\theta_{max})$ are found to be essentially featureless at the position of the coffee-beans. The diffraction angle between the incident and scattered X-ray photons almost does not change across the 2D sample plane. This diffraction angle is directly determined by the lattice parameter via the Bragg law. In our case, the lack of modulation in the diffraction angle of the (1, 0, 0) Bragg peak indicates all the local 1T-TaS_2 tiles share almost identical in-plane lattice parameters, a, even within the coffee-bean region. Also note the (0, 0, 1) axis of the 1T-TaS_2 tiles is known to be roughly normal to the supporting silicon wafer across the entire sample. Thus, any in-plane twist around the (0, 0, 1) axis could lead to the combination of $\delta(\theta_{max})$ and $\gamma(\theta_{max})$ to rotate along the Debye–Scherrer ring. The lack of such a motion means the local 1T-TaS_2 tiles are almost azimuthally aligned. Hence, the modulation in θ_{max} as shown in Figure 3a could only come from minor relative tilts between adjacent 1T-TaS_2 tiles along the c-axis. In this sense, our nanoXRD studies present an independent and self-contained survey of the local crystalline lattice.

We now piece together these tiles into a sheet of 1T-TaS_2. We expect the sample height function to be continuous, with the edges of neighboring tiles at the same sample height normal to the underlying silicon substrate. The difference in the sample height between the mathematically infinitesimal tiles is

$$\frac{\partial h(x,\ y)}{\partial x} = \tan \theta_{max}(x,\ y) \simeq \theta_{max}(x,\ y) \tag{1}$$

where $h(x, y)$ is the height of the sample along the z direction out of the quasi-2D plane and away from the underlying wafer. θ_{max} again is defined at each Bragg peak relative to the Bragg angle of the unperturbed region similar to elsewhere in this article. The x and y directions are parallel to the detector δ and γ angles at normal transmission, respectively. We integrate in the quasi-2D plane

$$h(x,\ y) = \int^{x} \theta_{max}(x',\ y)\, dx' \tag{2}$$

We derive the sample corrugation shown in Figure 3d. We can readily see that each of these coffee-bean shapes corresponds to a bubble-like, smooth one-sided deformation profile protruding above the substrate. Strictly speaking, eq 2 above only applies when the scattering plane is normal to the θ rotation axis (Bragg peak (1, 0, 0) for the specific sample). For all the Bragg peaks we explored, the scattering plane (defined by the incident X-ray and the combination of δ_{max} and γ_{max} angles) is always normal to the direction of the fine "meridional bar" connecting two-halves of the coffee bean in the corresponding intensity map shown in Figure 1. Where the scattering plane is tilted relative to the θ rotation axis, it could be mathematically shown that the 1D integration should be performed in the scattering plane.

Furthermore, these nanoXRD data are sufficient to allow direct calculation of the full strain tensor ε_{ij} from the deformation profile. We plot all the nonzero elements of the strain tensor in Figure 3e–i. Three of these terms, ε_{xx}, ε_{yy}, and ε_{xy} (and ε_{yx}), are proportional to θ_{max}^2, or effectively zero if we only keep terms linear in θ_{max}, reflecting extremely small changes in the lattice constants and d-spacings. This illustrates the high strain sensitivity of our nanoXRD method. $\varepsilon_{yz/zx}$ are linear in θ_{max} and are directly related to the sample rotation as we have so far ignored the thickness of our sample under the quasi-2D assumption.

We simulate the diffraction intensity of a Gaussian-like bubble protruding toward the incident X-ray at a series of θ rotations in Figure 4a–e, with the scattering plane containing the x-axis. Figure 4a–e is consistent with our experimental observations. Figure 4f–j presents the diffraction intensity maps with the scattering plane rotating 15° relative to the z-axis pointing out of the x–O–y plane. Note the "meridional bar" connecting the two halves of the "coffee-bean" is always orthogonal to and rotates with the scattering plane. The nanotiles along the "meridional bar" have their scattering vectors lying parallel to the scattering plane and thus have the maximum diffraction intensity. This effect has been experimentally observed as shown in Figure 1c–e.

The formation of these micron- and submicron-sized bubbles could be attributed in part to the intrinsic "softness" of these materials in the Mermin–Wagner sense. The Mermin–Wagner theorem[29] states that no long-range lattice order can exist in two dimensions because it is unstable to thermal fluctuations. Accordingly, perfect 2D materials in principle should not lie completely flat in the 2D plane but extend into the third dimension. As bulk materials become thinner toward the quasi-2D limit, it appears plausible that the materials also become more prone to the kind of corrugations presented in this work. Equally possible in our case, as the quasi-2D sheets are prepared at ambient pressure, a small

https://dx.doi.org/10.1021/acsami.0c06517
ACS Appl. Mater. Interfaces 2020, 12, 43173–43179

volume of gas may have been trapped underneath the sheet. nanoXRD was performed at around 0.3 bar helium gas environment, possibly leading to a net pressure difference between the two sides of the sheet. Under this assumption, the height h and the radii r of a nanobubble in the 2D plane follow $R^2 = r^2 + (R - h)^2$, where R is the curvature of the surface in 3D (Figure 3j inset). In our case, the distribution of bubble sizes is consistent with a 3D surface curvature $R \sim 0.3$ mm (Figure 3j). Given a pressure difference of 0.7 bar across the two sides of the bubble, Young's modulus can be estimated to be ~100 GPa for a strain of ~0.1%, which is 3 times the calculated value of bulk 1T-TaS_2,[30,31] but less than 50% of the Young's modulus measured from ultrathin MoS_2.[16] Details of the calculations can be found in the Supporting Information.

For the small strains ≪1% as measured in our sample, we observed that the distribution of the charge order is relatively uniform and follows the corrugation of the nanosheet. As the strain approaches a critical value around 3%, the electronic band structure deforms and will eventually suppress the charge order as the electron density of states cross the Fermi level, leading to alternative charge-scattering channels.[10]

CONCLUSIONS

We would like to compare our results with an electron diffraction version of strain mapping, which was recently demonstrated in refs 32 and 33. Major progress of that work, compared with previous scanning electron diffraction experiments, is to use a nano-sized electron source to avoid the complicated dynamical simulations needed for converging beam electron diffraction studies. However, these electron diffraction methods are severely limited by the penetration depth of electrons and, furthermore, require samples to be in a free-standing geometry. In comparison, nanoXRD is well poised to study materials sealed as a device, with a top gate and/or a substrate. The spatial resolution of our nanoXRD approach is limited by the focused X-ray beam size (80 nm in this work) and could be improved using smaller X-ray beams (sub 10 nm in a state-of-the-art nanodiffraction facility such as the one where this work was performed[18,19]) and also with the help of Bragg projection ptychographic reconstruction (1 nm as demonstrated in ref 23). Indeed, our spatial resolution still lags behind that of electron and atomic force microscopes. On the other hand, as ~10 keV X-ray photons have much smaller momentum than those of electrons in a typical electron microscope, nanoXRD generally features better strain sensitivity than its electron counterpart. As quasi-2D materials get thinner, current electron diffraction experiments are inherently even more limited to quantify the sample morphology in the third dimension, preventing a full description of the strain tensor. Admittedly, approaches similar to ours have been demonstrated at ESRF, but only for prepatterned model materials.[17−19] Here, we have managed to experimentally extract strain and Young's modulus in realistic quasi-2D materials with superior spatial resolution even in the absence of ptychographic reconstruction and will inspire future applications in obtaining crucial mechanical properties in these materials. The implications of our results will be significant when attempts are made in the future to assemble nanoscale heterostructures made from stacking quasi-2D materials on top of each other.[34] We suggest that nanoXRD could be a useful technique to understand the contacts formed between such quasi-2D materials and could have a significant impact in that field.

ASSOCIATED CONTENT

Supporting Information

The Supporting Information is available free of charge at https://pubs.acs.org/doi/10.1021/acsami.0c06517.

Bulk sample synthesis; nanoflake preparation; nanoXRD; and estimation of Young's modulus (PDF)

AUTHOR INFORMATION

Corresponding Authors

Yue Cao − *Condensed Matter Physics and Material Science Department, Brookhaven National Laboratory, Upton, New York 11973, United States; Materials Science Division, Argonne National Laboratory, Lemont, Illinois 60439, United States;* orcid.org/0000-0002-3989-158X; Email: yue.cao@anl.gov

Ian K. Robinson − *Condensed Matter Physics and Material Science Department, Brookhaven National Laboratory, Upton, New York 11973, United States*; Email: irobinson@bnl.gov

Authors

Tadesse Assefa − *Condensed Matter Physics and Material Science Department, Brookhaven National Laboratory, Upton, New York 11973, United States;* orcid.org/0000-0003-3904-0846

Soham Banerjee − *Condensed Matter Physics and Material Science Department, Brookhaven National Laboratory, Upton, New York 11973, United States; Department of Applied Physics and Applied Mathematics, Columbia University, New York, New York 10027, United States;* orcid.org/0000-0001-9271-493X

Andrew Wieteska − *Department of Physics, Columbia University, New York, New York 10027, United States*

Dennis Zi-Ren Wang − *Department of Applied Physics and Applied Mathematics, Columbia University, New York, New York 10027, United States*

Abhay Pasupathy − *Department of Physics, Columbia University, New York, New York 10027, United States; Condensed Matter Physics and Material Science Department, Brookhaven National Laboratory, Upton, New York 11973, United States;* orcid.org/0000-0002-2744-0634

Xiao Tong − *Center for Functional Nanomaterials (CFN), Brookhaven National Laboratory, Upton, New York 11973, United States*

Yu Liu − *Key Laboratory of Materials Physics, Institute of Solid State Physics, Chinese Academy of Sciences, Hefei 230031, People's Republic of China*

Wenjian Lu − *Key Laboratory of Materials Physics, Institute of Solid State Physics, Chinese Academy of Sciences, Hefei 230031, People's Republic of China*

Yu-Ping Sun − *Key Laboratory of Materials Physics, Institute of Solid State Physics and High Magnetic Laboratory, Chinese Academy of Sciences, Hefei 230031, People's Republic of China; Collaborative Innovation Centre of Advanced Microstructures, Nanjing University, Nanjing 210093, People's Republic of China*

Yan He − *Shanghai Synchrotron Radiation Facility (SSRF), Shanghai Institute of Applied Physics, Chinese Academy of Sciences, Shanghai 201800, P. R. China*

Xiaojing Huang − *National Synchrotron Light Source II, Brookhaven National Laboratory, Upton, New York 11973, United States*

Hanfei Yan − *National Synchrotron Light Source II, Brookhaven National Laboratory, Upton, New York 11973, United States*

https://dx.doi.org/10.1021/acsami.0c06517
ACS Appl. Mater. Interfaces 2020, 12, 43173−43179

Yong S. Chu − *National Synchrotron Light Source II, Brookhaven National Laboratory, Upton, New York 11973, United States*

Simon J. L. Billinge − *Condensed Matter Physics and Material Science Department, Brookhaven National Laboratory, Upton, New York 11973, United States; Department of Applied Physics and Applied Mathematics, Columbia University, New York, New York 10027, United States;* orcid.org/0000-0002-9734-4998

Complete contact information is available at: https://pubs.acs.org/10.1021/acsami.0c06517

Author Contributions

Y.C., I.K.R., S.B., and S.J.L.B. conceived the experiment. Y.C., T.A., S.B., Y.H., X.H., H.Y., and Y.S.C performed the nanoXRD measurement. Y.L., W.L., and Y.-P.S. grew the bulk 1T-TaS_2 crystals. S.B., A.W., D.Z.-R.W., and A.P. further prepared the thin 1T-TaS_2 flakes used in the nanoXRD experiments. X.T. performed the AFM characterization. Data analysis and interpretation was carried out by Y.C, I.K.R, and S.J.L.B. Y.C. and I.K.R. wrote the majority of the article with input from all coauthors.

Notes

The authors declare no competing financial interest.

■ ACKNOWLEDGMENTS

Y.C. thanks Jing Tao, Jun Li, and Chang-Yong Nam for valuable discussions and acknowledges Stephan O. Hruszkewycz and Martin Holt for helpful earlier explorations. The work at Brookhaven National Laboratory and Columbia University was supported by the U.S. Department of Energy, Office of Basic Energy Sciences, Division of Materials Sciences and Engineering, under contract no. DE-SC0012704. The work at Argonne National Laboratory was supported by the U.S. Department of Energy, Office of Basic Energy Sciences, under contract no. DE-AC0206CH11357. This research used Beamline 3-ID HXN (Hard X-ray Nanoprobe) of the National Synchrotron Light Source II, a U.S. Department of Energy (DOE) Office of Science User Facilities operated for the DOE Office of Science by Brookhaven National Laboratory under contract no. DE-SC0012704. Sample characterization was carried out using resources at the Center for Functional Nanomaterials, which is a U.S. DOE Office of Science Facility, at Brookhaven National Laboratory under contract no. DE-SC0012704. S.B. acknowledges support from the National Defense Science and Engineering Graduate Fellowship (DOD-NDSEG) program. D.-Z.R.W. is funded by the Department of Energy under contract no. DE-SC0016703. Y.L., W.L., and Y.-P.S. acknowledge support from the National Key Research and Development Program (grant 2016YFA0300404), the National Nature Science Foundation of China (grants 11674326, 11774352, and 11874357), the Joint Funds of the National Natural Science Foundation of China, and the Chinese Academy of Sciences' Large-scale Scientific Facility (Grant U1832141). Y.H. is supported by the Natural Science Foundation of Shanghai (17ZR1436800).

■ REFERENCES

(1) Ohta, T.; Bostwick, A.; McChesney, J. L.; Seyller, T.; Horn, K.; Rotenberg, E. Interlayer Interaction and Electronic Screening in Multilayer Graphene Investigated with Angle-Resolved Photoemission Spectroscopy. *Phys. Rev. Lett.* **2007**, *98*, 206802.

(2) Zhang, Y.; Chang, T.-R.; Zhou, B.; Cui, Y.-T.; Yan, H.; Liu, Z.; Schmitt, F.; Lee, J.; Moore, R.; Chen, Y.; Lin, H.; Jeng, H.-T.; Mo, S.-K.; Hussain, Z.; Bansil, A.; Shen, Z.-X. Direct Observation of the Transition from Indirect to Direct Bandgap in Atomically Thin Epitaxial MoSe2. *Nat. Nanotechnol.* **2014**, *9*, 111−115.

(3) Ugeda, M. M.; Bradley, A. J.; Shi, S.-F.; da Jornada, F. H.; Zhang, Y.; Qiu, D. Y.; Ruan, W.; Mo, S.-K.; Hussain, Z.; Shen, Z.-X.; Wang, F.; Louie, S. G.; Crommie, M. F. Giant Bandgap Renormalization and Excitonic Effects in a Monolayer Transition Metal Dichalcogenide Semiconductor. *Nat. Mater.* **2014**, *13*, 1091−1095.

(4) He, J.; Hummer, K.; Franchini, C. Stacking Effects on the Electronic and Optical Properties of Bilayer Transition Metal Dichalcogenides MoS2, MoSe2, WS2, and WSe2. *Phys. Rev. B: Condens. Matter Mater. Phys.* **2014**, *89*, 075409.

(5) Naumis, G. G.; Barraza-Lopez, S.; Oliva-Leyva, M.; Terrones, H. Electronic and Optical Properties of Strained Graphene and Other Strained 2D Materials: a Review. *Rep. Prog. Phys.* **2017**, *80*, 096501.

(6) Johannes, M. D.; Mazin, I. I. Fermi Surface Nesting and the Origin of Charge Density Waves in Metals. *Phys. Rev. B: Condens. Matter Mater. Phys.* **2008**, *77*, 165135.

(7) Liu, A. Y. Electron-Phonon Coupling in Compressed 1T-TaS2: Stability and Superconductivity from First Principles. *Phys. Rev. B: Condens. Matter Mater. Phys.* **2009**, *79*, 220515.

(8) Ge, Y.; Liu, A. Y. First-Principles Investigation of the Charge-Density-Wave Instability in 1T-TaSe2. *Phys. Rev. B: Condens. Matter Mater. Phys.* **2010**, *82*, 155133.

(9) Vaskivskyi, I.; Gospodaric, J.; Brazovskii, S.; Svetin, D.; Sutar, P.; Goreshnik, E.; Mihailovic, I. A.; Mertelj, T.; Mihailovic, D. Controlling the Metal-to-Insulator Relaxation of the Metastable Hidden Quantum State in 1T-TaS2. *Sci. Adv.* **2015**, *1*, No. e1500168.

(10) Gan, L.-Y.; Zhang, L.-H.; Zhang, Q.; Guo, C.-S.; Schwingenschlögl, U.; Zhao, Y. Strain Tuning of the Charge Density Wave in Monolayer and Bilayer 1T-TaS2. *Phys. Chem. Chem. Phys.* **2016**, *18*, 3080−3085.

(11) Zhao, R.; Wang, Y.; Deng, D.; Luo, X.; Lu, W. J.; Sun, Y.-P.; Liu, Z.-K.; Chen, L.-Q.; Robinson, J. Tuning Phase Transitions in 1T-TaS2 via the Substrate. *Nano Lett.* **2017**, *17*, 3471−3477.

(12) Sipos, B.; Kusmartseva, A. F.; Akrap, A.; Berger, H.; Forró, L.; Tutiš, E. From Mott State to Superconductivity in 1T-TaS2. *Nat. Mater.* **2008**, *7*, 960−965.

(13) Lee, C.; Wei, X.; Kysar, J. W.; Hone, J. Measurement of the Elastic Properties and Intrinsic Strength of Monolayer Graphene. *Science* **2008**, *321*, 385−388.

(14) Cooper, R. C.; Lee, C.; Marianetti, C. A.; Wei, X.; Hone, J.; Kysar, J. W. Nonlinear Elastic Behavior of Two-Dimensional Molybdenum Disulfide. *Phys. Rev. B: Condens. Matter Mater. Phys.* **2013**, *87*, 035423.

(15) Bunch, J. S.; Van Der Zande, A. M.; Verbridge, S. S.; Frank, I. W.; Tanenbaum, D. M.; Parpia, J. M.; Craighead, H. G.; McEuen, P. L. Electromechanical Resonators from Graphene Sheets. *Science* **2007**, *315*, 490−493.

(16) Bertolazzi, S.; Brivio, J.; Kis, A. Stretching and Breaking of Ultrathin MoS2. *ACS Nano* **2011**, *5*, 9703−9709.

(17) Chahine, G. A.; Richard, M.-I.; Homs-Regojo, R. A.; Tran-Caliste, T. N.; Carbone, D.; Jacques, V. L. R.; Grifone, R.; Boesecke, P.; Katzer, J.; Costina, I.; Djazouli, H.; Schroeder, T.; Schülli, T. U. Imaging of Strain and Lattice Orientation by Quick Scanning X-ray Microscopy Combined with Three-Dimensional Reciprocal Space Mapping. *J. Appl. Crystallogr.* **2014**, *47*, 762−769.

(18) Leake, S. J.; Chahine, G. A.; Djazouli, H.; Zhou, T.; Richter, C.; Hilhorst, J.; Petit, L.; Richard, M.-I.; Morawe, C.; Barrett, R.; Zhang, L.; Homs-Regojo, R. A.; Favre-Nicolin, V.; Boesecke, P.; Schülli, T. U. The Nanodiffraction Beamline ID01/ESRF: a Microscope for Imaging Strain and Structure. *J. Synchrotron Radiat.* **2019**, *26*, 571−584.

(19) Richard, M.-I.; Zoellner, M. H.; Chahine, G. A.; Zaumseil, P.; Capellini, G.; Häberlen, M.; Storck, P.; Schülli, T. U.; Schroeder, T. Structural Mapping of Functional Ge Layers Grown on Graded SiGe

Buffers for sub-10 nm CMOS Applications Using Advanced X-ray Nanodiffraction. *ACS Appl. Mater. Interfaces* **2015**, *7*, 26696−26700.
(20) Chen, X. M.; Miller, A.; Nugroho, C.; de la Peña, G.; Joe, Y.; Kogar, A.; Brock, J.; Geck, J.; MacDougall, G.; Cooper, S.; Fradkin, E.; Van Harlingen, D. J.; Abbamonte, P. Influence of Ti Doping on the Incommensurate Charge Density Wave in 1T-TaS2. *Phys. Rev. B: Condens. Matter Mater. Phys.* **2015**, *91*, 245113.
(21) Yan, H.; Bouet, N.; Zhou, J.; Huang, X.; Nazaretski, E.; Xu, W.; Cocco, A. P.; Chiu, W. K. S.; Brinkman, K. S.; Chu, Y. S. Multimodal Hard X-ray Imaging with Resolution Approaching 10 nm for Studies in Material Science. *Nano Futures* **2018**, *2*, 011001.
(22) Nazaretski, E.; Yan, H.; Lauer, K.; Bouet, N.; Huang, X.; Xu, W.; Zhou, J.; Shu, D.; Hwu, Y.; Chu, Y. S. Design and Performance of an X-ray Scanning Microscope at the Hard X-ray Nanoprobe Beamline of NSLS-II. *J. Synchrotron Radiat.* **2017**, *24*, 1113−1119.
(23) Godard, P.; Carbone, G.; Allain, M.; Mastropietro, F.; Chen, G.; Capello, L.; Diaz, A.; Metzger, T. H.; Stangl, J.; Chamard, V. Three-Dimensional High-Resolution Quantitative Microscopy of Extended Crystals. *Nat. Commun.* **2011**, *2*, 568.
(24) Takahashi, Y.; Suzuki, A.; Furutaku, S.; Yamauchi, K.; Kohmura, Y.; Ishikawa, T. Bragg X-ray Ptychography of a Silicon Crystal: Visualization of the Dislocation Strain Field and the Production of a Vortex Beam. *Phys. Rev. B: Condens. Matter Mater. Phys.* **2013**, *87*, 121201.
(25) Holt, M. V.; Hruszkewycz, S. O.; Murray, C. E.; Holt, J. R.; Paskiewicz, D. M.; Fuoss, P. H. Strain Imaging of Nanoscale Semiconductor Heterostructures with X-Ray Bragg Projection Ptychography. *Phys. Rev. Lett.* **2014**, *112*, 165502.
(26) Hruszkewycz, S. O.; Allain, M.; Holt, M. V.; Murray, C. E.; Holt, J. R.; Fuoss, P. H.; Chamard, V. High-Resolution Three-dimensional Structural Microscopy by Single-Angle Bragg Ptychography. *Nat. Mater.* **2017**, *16*, 244−251.
(27) Lohmeier, M.; Vlieg, E. Angle Calculations for a Six-Circle Surface X-ray Diffractometer. *J. Appl. Crystallogr.* **1993**, *26*, 706−716.
(28) Huang, X.; Lauer, K.; Clark, J. N.; Xu, W.; Nazaretski, E.; Harder, R.; Robinson, I. K.; Chu, Y. S. Fly-Scan Ptychography. *Sci. Rep.* **2015**, *5*, 9074.
(29) Mermin, N. D.; Wagner, H. Absence of Ferromagnetism or Antiferromagnetism in One- or Two-Dimensional Isotropic Heisenberg Models. *Phys. Rev. Lett.* **1966**, *17*, 1133−1136.
(30) de Jong, M.; Chen, W.; Angsten, T.; Jain, A.; Notestine, R.; Gamst, A.; Sluiter, M.; Ande, C. K.; van der Zwaag, S.; Plata, J. J.; Toher, C.; Curtarolo, S.; Ceder, G.; Persson, K. A.; Asta, M. Charting the Complete Elastic Properties of Inorganic Crystalline Compounds. *Sci. Data* **2015**, *2*, 150009.
(31) Materials project. https://materialsproject.org/materials/mp-1690/ (accessed April 4, 2020).
(32) Ozdol, V. B.; Gammer, C.; Jin, X. G.; Ercius, P.; Ophus, C.; Ciston, J.; Minor, A. M. Strain Mapping at Nanometer Resolution using Advanced Nano-beam Electron Diffraction. *Appl. Phys. Lett.* **2015**, *106*, 253107.
(33) Han, Y.; Nguyen, K.; Cao, M.; Cueva, P.; Xie, S.; Tate, M. W.; Purohit, P.; Gruner, S. M.; Park, J.; Muller, D. A. Strain Mapping of Two-Dimensional Heterostructures with Subpicometer Precision. *Nano Lett.* **2018**, *18*, 3746−3751.
(34) Geim, A. K.; Grigorieva, I. V. Van der Waals Heterostructures. *Nature* **2013**, *499*, 419−425.

https://dx.doi.org/10.1021/acsami.0c06517
ACS Appl. Mater. Interfaces 2020, 12, 43173−43179